Available online at www.sciencedirect.com
ScienceDirect
International Journal of Thermal Sciences 48 (2009) 234–242
International Journal of Thermal Sciences
www.elsevier.com/locate/ijts

Numerical study on the formation of Taylor bubbles in capillary tubes

Yuming Chen *, Rudi Kulenovic, Rainer Mertz

University of Stuttgart, Institute of Nuclear Technology and Energy Systems (IKE), Pfaffenwalding 31, Stuttgart 70569, Germany

Received 14 September 2007; received in revised form 27 December 2007; accepted 3 January 2008

Available online 30 January 2008

Abstract

Numerical simulations have been carried out for the transient formation of Taylor bubbles in a nozzle/tube co-flow arrangement by solving the unsteady, incompressible Navier–Stokes equations. A level set method was used to track the two-phase interface. The calculated bubble size, shape, liquid film thickness, bubble length, drift velocity, pressure drop and flow fields of Taylor flow agree well with the literature data. For a given nozzle/tube configuration, the formation of Taylor bubbles is found to be mainly dependent on the relative magnitude of gas and liquid superficial velocity. However, even under the same liquid and gas superficial velocities, the change of nozzle geometry alone can drastically change the size of Taylor bubbles and the pressure drop behavior inside a given capillary. This indicates that the widely used flow pattern map presented in terms of liquid and gas superficial velocities is not unique.

Keywords: Taylor bubble; Capillary tubes; Liquid co-flow; Numerical simulation; Bubble departure diameter; Pressure drop; Bubble shape

1. Introduction

Taylor flow is a dominant flow pattern in capillary tubes for small to medium gas and liquid superficial velocities, which is a special case of slug flow where the bullet-shaped (Taylor) bubbles are separated by liquid slugs with no gas entrained. It has been shown that the hydrodynamics of Taylor flow allows a good heat and mass transfer between bubbles and slugs and between bubbles and channel wall [1]. Therefore, the study of Taylor flow in capillary tubes is of great interest, particularly in the areas of microfluidics and microreactors.

The steady-state propagation of a semi-infinite air finger (or long air bubble) in a viscous fluid in a 2D channel (Bretherton's problem) has been intensively studied. For small Reynolds numbers, the system behavior is governed by a balance between viscous and capillary forces. The inertia was usually assumed to be of minor importance. The liquid film formed between the bubble and the channel wall has a uniform thickness (δ) which is given by Bretherton [2] as

$$\delta/D_t = 0.66Ca^{2/3} \tag{1}$$

where, D_t is the tube diameter and Ca is the capillary number. Eq. (1) is applicable for $Ca \ll 1$. For a larger Ca, Taylor's experimental data [3] was generally used for comparison. It has been shown that a constant liquid film also exists for cases of finite Reynolds numbers [4]. Due to the presence of liquid film, the bubble moves faster than the liquid slug. Fairbrother and Stubbs [5] suggested an empirical correlation for the relative bubble drift velocity given by

$$(U_b - U_s)/U_s = 1.0Ca^{1/2} \tag{2}$$

Bretherton's solution [2] for small Ca is written

$$(U_b - U_s)/U_s = 1.29(3Ca)^{2/3} \tag{3}$$

Here U_s is the slug velocity. For vertical tubes, a correction was introduced to Eq. (3) using a factor $(1 \pm 2/3Bo)$ for upward and downward flows, respectively [2] ($Bo = \rho g R_t^2/\sigma$, is the Bond number with R_t representing the tube radius).

According to Taylor [3], for a relative drift velocity (the left-hand side of Eq. (2)) greater than 0.5, a complete bypass flow pattern is expected in front of the Taylor bubble, otherwise, stagnant points would occur inside the bubble and/or slug. This suggests a possible recirculation flow inside the slug. Several numerical simulations [4,6,7] and PIV visualization [8] show the existence of the recirculation flow inside the slugs. However, all these results, both from the numerical calculations and

* Corresponding author. Fax: +49 711 68562010.
E-mail address: yuming.chen@ike.uni-stuttgart.de (Y. Chen).

1290-0729/$ – see front matter
doi:10.1016/j.ijthermalsci.2008.01.004

Nomenclature

Bo	$= \rho g R_t^2/\sigma$, bond number
Ca	$= \mu U_b/\sigma$, capillary number
D	diameter
Fr	$= U^2/(gL)$, Froude number
g	gravitational constant
h	grid spacing
H	Heaviside function
L	reference length
t	time
p	pressure
Q	gas flow rate
R	radius
R_i	inner radius of nozzle
R_o	outer radius of nozzle
Re	$= \rho_L U L/\mu_L$, Reynolds number
u	x-component velocity
U	reference velocity
U_{sg}	superficial gas velocity
U_{sl}	superficial liquid velocity
$\vec{w}$	velocity vector
We	$= \rho_L U^2 L/\sigma$, Weber number

Greek letters

δ	liquid film thickness, delta function
ϕ	level set function
κ	curvature
λ	slip length
μ	viscosity
θ	contact angle
ρ	density
σ	surface tension

Subscripts

ad	advancing
b	bubble
ct	contact line
max	maximum
re	receding
s	slug
t	tube

the experiments, were obtained with a reference frame moving at the bubble or slug velocity. It is not clear if and under which conditions the recirculations inside the slugs exist.

Due to the changes in the flow field, there is a pressure drop across the Taylor bubble. This pressure drop increases with the Reynolds number [9]. Kreutzer et al. [6] experimentally studied the pressure drop of Taylor flow in capillaries for $Re \gg 1$. They found that for a slug length less than 10 times the tube diameter, the length-averaged friction factor increases dramatically over the single phase value. They also simulated the Taylor flow using a commercial CFD code for Re up to 900. The frictional pressure drop increases significantly with Re. The numerical calculations, however, under-predict the experimental friction factor by a factor of 2.5 for $Re > 50$.

Traditionally, the adiabatic two-phase flows (including the Taylor flows) are generated through a pre-mixer where the gas and liquid are mixed before entering the main channels. Only a few studies concern the formation of the Taylor flows in a co-flow nozzle/tube arrangement, where the bubbles are formed through a nozzle and the liquid is introduced through the annular channel between the nozzle and the tube [10,11]. Numerically, the Taylor flows are generally studied for the steady-state conditions and for long bubbles. Most of the numerical studies neglect the viscous and inertial effects of the gas phase (by assuming a constant gas pressure), and many do not consider the gravity force, e.g., [4,6].

This paper concerns the numerical study on the transient formation of Taylor bubbles in a capillary tube with the co-flow arrangement mentioned above. For simulating highly deformable interfaces, the Eulerian interface-capturing methods such as volume-of fluid (VOF) method and the level set methods are most suitable. The VOF method was used in [7] to study the slug flow implemented in a commercial CFD package. The VOF method is naturally mass-conservative, since the volume fraction of a particular phase is tracked rather then the interface position. However, this method requires a complicated geometric calculation procedure, e.g., using a piecewise linear interface calculation (PLIC) algorithm, and it is thus difficult to extend to complex and three-dimensional topological changes. In this study, the level set method is adopted to track the two-phase interface which was first introduced by Osher and Sethian [12] and later extended to incompressible two-phase flow by Sussman and his co-workers [13,14]. The main advantage of the level set method is its simplicity, since interface normals, curvature and distance towards the interface can be expressed easily in terms of the level set function. Furthermore, this method allows for simulating multiphase flows with large jump in density and viscosity across the interfaces. The mass loss (or gain) is the main problem for the level set method in certain situations, e.g., in studying free rising bubbles. In this study the rate of mass loss is negligible (less than 1%) compared to imposed gas flow rate, therefore it is not a least concern.

2. Numerical scheme

2.1. Level set method

In the level set method, a continuous function ϕ is introduced over the whole computational domain. This level set function is given the property of a distance function indicating the shortest distance to the interface. Thus, the zero level set of the function ($\phi = 0$) represents the interface. We take $\phi < 0$ in the gas region and $\phi > 0$ in the liquid region. The advection of ϕ is given by

$$\frac{\partial \phi}{\partial t} + \vec{w} \cdot \nabla \phi = 0 \tag{4}$$

where $\vec{w}$ is the velocity of the interface. The physical properties are assumed constant in each phase, they take different values depending on the sign of ϕ. To avoid a sudden jump of the material properties across the interface, which can have a substantial effect on the stability of the numerical scheme, we define a smoothed Heaviside function [13]

$$H(\phi) = \begin{cases} 0 & \text{if } \phi < -\varepsilon \\ 0.5[1 + \phi/\varepsilon - \sin(\pi\phi/\varepsilon)/\pi] & \text{if } |\phi| \leqslant \varepsilon \\ 1 & \text{if } \phi > \varepsilon \end{cases} \tag{5}$$

In the calculation $\varepsilon = 3h/2$ is taken (h is the grid spacing). A smoothed material property γ, e.g., density, viscosity, etc., is then calculated by

$$\gamma(\phi) = \gamma_L H(\phi) + \gamma_V \big(1 - H(\phi)\big) \tag{6}$$

It is known that under the evolution of Eq. (4), ϕ will not necessarily remain a distance function. Therefore, the re-distance techniques proposed by Sussman et al. [13,14] are used to maintain ϕ as a distance function without changing its zero level set.

2.2. Governing equations

We solve the unsteady, incompressible Navier–Stokes equations for laminar flows in a 2D axisymmetric coordinate system. The non-dimensional governing equations are

$$\nabla \cdot \vec{w} = 0 \tag{7}$$

$$\frac{\partial \vec{w}}{\partial t} + \frac{\nabla p}{\rho} = -\vec{w} \cdot \nabla \vec{w} + \frac{1}{Fr}\vec{g} + \frac{1}{\rho Re}\big[\nabla \cdot (\mu \nabla \vec{w}) + \nabla \cdot (\mu \nabla \vec{w}^T)\big] + \frac{\kappa \delta \nabla \phi}{\rho We} = F^n \tag{8}$$

Here the continuous surface force model [15] is used. δ is a delta function given by the relation $\nabla H = \delta \nabla \phi$. The Navier–Stokes equations are solved using the projection method of Chorin [16]. In this method an intermediate velocity field $\vec{w}^*$ is first calculated which is generally not divergence free, then the pressure at the next time level is calculated that ensures the velocity field satisfies the continuity equation. The projection step is given by

$$(\vec{w}^* - \vec{w}^n)/\Delta t = F^n \tag{9}$$

Here F^n represents the right-hand side of Eq. (8) which is calculated explicitly at the time step n. With Eq. (9), the time-discrete Navier–Stokes equations can be written as (the correction step)

$$(\vec{w}^{n+1} - \vec{w}^*)/\Delta t + \nabla p^{n+1}/\rho(\phi^{n+1}) = 0 \tag{10}$$

The pressure at the next time step $(n+1)$ is found by taking the divergence of Eq. (10), and using Eq. (7), yielding the pressure Poisson equation (PPE):

$$\nabla \cdot \big(\nabla p^{n+1}/\rho(\phi^{n+1})\big) = \nabla \cdot \vec{w}^*/\Delta t \tag{11}$$

The homogeneous Neumann boundary conditions are obtained for the PPE by projecting Eq. (10) onto the outer unit normal of the domain boundary and setting $\vec{w}^*_\Gamma = \vec{w}^{n+1}_\Gamma$ (Γ represents the boundary). After solving Eq. (11) for the new pressure, the velocities at the new time step $\vec{w}^{n+1}$ are calculated by Eq. (10).

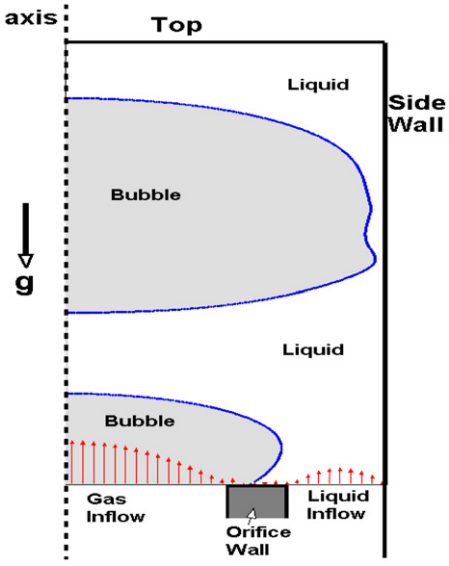

Fig. 1. Calculation domain and boundaries.

2.3. Discretization

The finite difference scheme is applied on a 2D staggered (MAC) grid system with uniform grid spacing h. The pressure and level set functions are defined at the cell centers (i, j), while the velocities are defined at the cell faces, i.e. $u_{i+1/2,j}$ and $v_{i,j+1/2}$. Therefore, the projection and correction equations are solved on the cell faces and the pressure Poisson equation is solved at the cell centers. The time derivatives in Eqs. (4) and (9) are approximated with a second order Adams–Bashford scheme. A fifth order WENO scheme [17] is adopted for the treatment of the convection terms in the momentum equations (Eq. (8)) and the advection equation for the level set function (Eq. (4)). The viscous and curvature terms are discretized using central difference scheme. We employ a Bi-CGSTAB method with ILU preconditioner for solving the PPE (Eq. (11)).

2.4. Initial and boundary conditions

The calculation domain is a half cylinder (Fig. 1), with length at least 10 times greater than the tube radius. For the velocity boundaries, symmetric conditions for the axis and no-slip conditions for the right boundary (tube wall) are used. Out-flow conditions are imposed at top boundary (tube outlet). In some cases, we prescribe the Hagen–Poiseuille velocity profile at the outlet with a mean velocity equal to inlet two-phase velocity. As long as the outlet is sufficiently far away from the nearest bubble interface the two kinds of outlet boundary conditions essentially give the same results. For the bottom boundary, we prescribe the fully developed tubular and annular velocity profiles for the gas inlet and liquid inlet, respectively. For the orifice ring wall a no-penetration condition is imposed for the normal velocity component and the Navier slip condition is used for the tangential velocity component, i.e. $u_{\text{slip}} = -\lambda(\partial u/\partial y)|_{\text{wall}}$. Here, u_{slip} is the slip velocity on the wall and λ is the slip length. Typically $\lambda = 0.5h$ is used (h is the grid spacing).

For the level set function, symmetric conditions are used for the axis and the right boundaries and an interpolation scheme is used for the bottom and top boundaries. The two velocity components are initially set to zero. The initial bubble is set to be a hemisphere centered on the middle of the orifice mouth, thus the initial level set function can be easily determined.

2.5. Contact line model

Special treatment of the contact line movement is needed due to the hysteresis and the dynamic nature of the contact angle. Generally, the apparent contact angle is linearly related to the contact line velocity (u_{ct}). In addition, the Navier slip condition is applied on the wall. This kind of model has been commonly used for macroscopic simulations [18,19]. In this calculation, similar to the procedure given in [20], the instantaneous apparent contact angle θ is set to vary linearly between the prescribed receding angle θ_{re} and the advancing angle θ_{ad} if the instantaneous contact line velocity u_{ct} is within a given maximum, $\pm u_{ct,max}$. Beyond this range, the contact angle is assigned by the value of θ_{ad} or θ_{re}, depending on the sign of contact line velocity, namely

$$\theta = \begin{cases} \theta_{re} & \text{if } u_{ct} < -u_{ct,max} \\ \theta_{re} + (\theta_{ad} - \theta_{re})\frac{u_{ct}+u_{ct,max}}{2u_{ct,max}} & \text{if } |u_{ct}| \leqslant u_{ct,max} \\ \theta_{ad} & \text{if } u_{ct} > u_{ct,max} \end{cases} \quad (12)$$

At the inner rim of the orifice wall, the contact angle is allowed to have any value between θ_{re} and 180°. Physically, the orifice edge is generally rounded (not in an ideal right angle), the apparent angle can be up to a value of $(90° + \theta_{ad})$. Numerically, this condition does not allow the contact line to recede into the orifice.

We found that the direct use of the above scheme imposes a severe time step restriction and requires a high mesh resolution. Furthermore, the relationship between the contact line velocity and the contact angle prescribed by Eq. (12) could cause physically impossible behavior on the contact line, that is the contact point can move backwards even when the contact line velocity is positive, or vice versa. Therefore, further restrictions are imposed: when the contact line velocity is positive while the contact point moves backwards, the contact position is set to the same position as in the former time step, and the contact angle is recalculated accordingly. The same procedure is used for the opposite case.

In [21], we presented a stick-slip model, where the contact line is set to move only when the contact angle exceeds the range limited by the prescribed receding and advancing angles. In fact, for the cases studied in this paper, the discrepancy introduced by using different contact line models is negligible, because the contact line tends to stick on or near the nozzle mouth due to the small nozzle wall thickness and the liquid co-flow [21].

3. Results and discussions

The calculation examples shown in this paper are all for the co-flow tube/nozzle arrangement (Fig. 1), with a tube inner diameter of 1 mm, a nozzle inner diameter of 0.34 mm and outer diameter of 0.64 mm. In Section 3.4 the effects of nozzle geometry will be presented. The dispersed phase is air and the continuous phase is octane ($\rho = 703$ kg/m^3, $\mu = 0.00085$ Pa s, $\sigma = 0.02149$ N/m). These geometries and working fluids are chosen in order to compare with the experiments of Salman et al. [11]. Air and octane are introduced into the channel with constant flow rates and fully developed velocity profiles. These conditions are also satisfied for the experiments in [11] where the nozzle length is more than 300 times the nozzle inner diameter.

3.1. Numerical verifications

The contact line model can strongly influence the predicted bubble departure size for bubble formation in a quiescent liquid [21]. Based on the model given in Section 2.5, the contact line movement is directly affected by the advancing angle θ_{ad}, the receding angle θ_{re}, the maximum contact line velocity $u_{ct,max}$, and indirectly by the slip length λ, grid spacing h and time step interval. The effects of these parameters on the bubble formation are shown in Table 1. It turns out that, for bubble formation in a co-flowing liquid, the contact line movement has little effect on bubble formation. From Table 1, even if these parameters vary dramatically, the maximum variation of the calculated bubble departure diameter is less than 1%.

For the following calculations, we use a grid spacing of 1/60 mm. The time step interval is determined according to CFL conditions, normally 1 to 2 μs. The advancing contact angle is set to 90 degrees, and the receding angle is 40 degrees, according to the photo shown in [11]. We take a maximum contact line velocity, $u_{ct,max} = 0.2$ m/s based on the experiments in [22]. The slip length $\lambda = 0.5h$ is used. The vertical length of the domain is at least 10 times the horizontal length.

The calculated bubble formation time and departure diameter are compared with the experimental data from [11] (only available for the low velocity range), as shown in Fig. 2. The agreement between calculations and experiments is excellent. The calculated bubble shapes also agree well with the photos shown in [11].

Table 1
Summary of numerical dependency study (physical domain size 0.5 × 2.5 mm^2)

h (mm)	Time step (μs)	θ_{ad}/θ_{re} (deg.)	λ	$u_{ct,max}$ (m/s)	D_b (mm)	Deviation (%)
1/60	**1.5**	**90 / 40**	**0.5*h***	**0.2**	**1.1781**	**0**
1/40	1.5	90 / 40	0.5*h*	0.2	1.1756	−0.21
1/80	1.5	90 / 40	0.5*h*	0.2	1.1771	−0.08
1/60	***0.75***	90 / 40	0.5*h*	0.2	1.1785	0.03
1/60	1.5	***80 / 50***	0.5*h*	0.2	1.1752	−0.25
1/60	1.5	***70 / 60***	0.5*h*	0.2	1.1690	−0.77
1/60	1.5	90 / 40	***0.1h***	0.2	1.1778	−0.03
1/60	1.5	90 / 40	***2.0h***	0.2	1.1784	0.03
1/60	1.5	90 / 40	0.5*h*	***0.05***	1.1803	0.19
1/60	1.5	90 / 40	0.5*h*	***0.5***	1.1729	−0.44

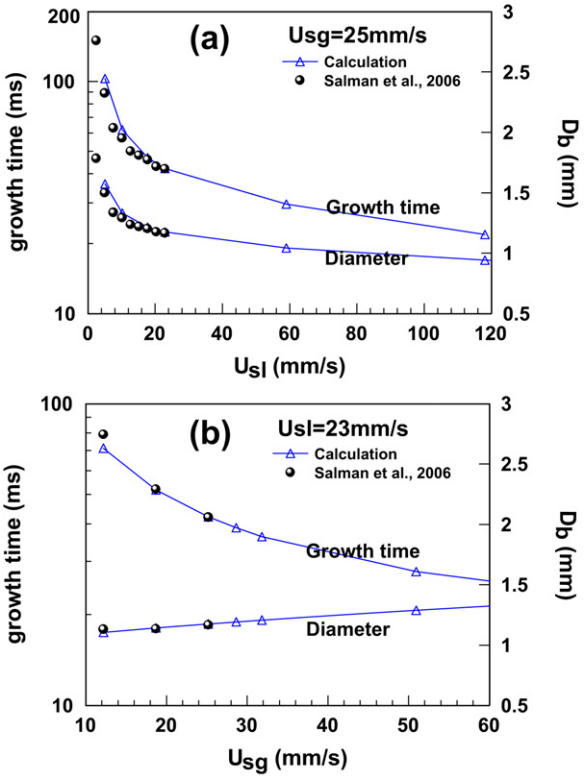

Fig. 2. Comparison between calculated and experimental bubble formation time and departure diameter for air/octane system.

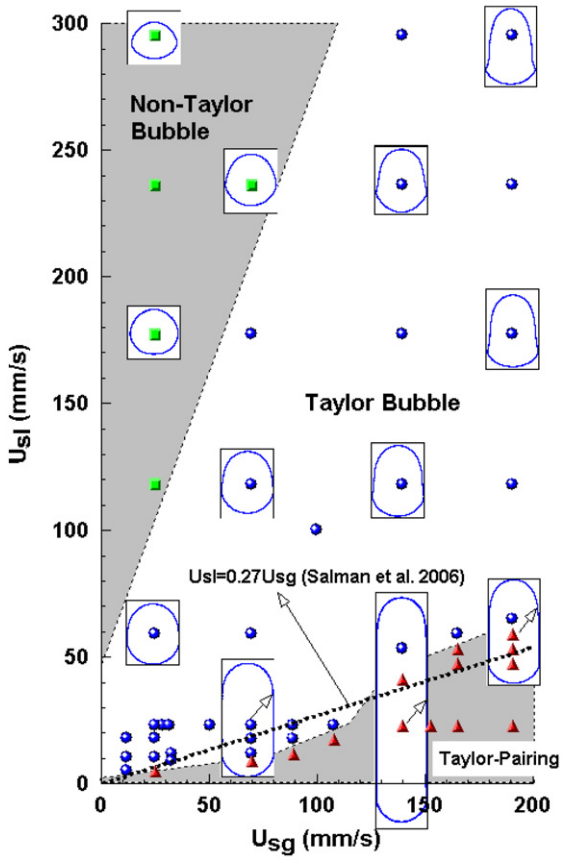

Fig. 3. Flow patterns and boundary of Taylor-pairing.

3.2. Bubble departure diameter under liquid co-flow

Under liquid co-flow, the contact line behavior is strongly influenced by the co-flow velocity and the gas inflow velocity. The increase of the liquid co-flow velocity reduces the maximum contact radius of the growing bubble. Surprisingly, at relatively high gas inflow velocity, the maximum contact radius also becomes smaller. For example, for a liquid superficial velocity (U_{sl}) of 118 mm/s, with increasing gas superficial velocity (U_{sg}) from 25 to 140 mm/s, the maximum contact radius decreases from 0.297 to 0.223 mm. In an infinite liquid pool, the increase of the maximum contact radius leads to a substantial increase of the bubble departure size. However, for Taylor bubble formation inside capillaries, the maximum contact radius has no clear effect on the departure diameter. This is because the necking process does not take place between the free expanding bubble front and the contact line, rather the main Taylor bubble body is reshaped by the tube wall.

The bubble departure size in capillaries under liquid co-flow mainly depends on the liquid and gas superficial velocities. The departure diameter increases with increasing gas superficial velocity and decreasing liquid superficial velocity. This can be roughly seen in Fig. 3 where the calculated flow patterns are shown for a liquid superficial velocity ranging from 0.005 to 0.3 m/s and a gas superficial velocity from 0.01 to 0.2 m/s. Due to the strong capillary effects, it is well known that the flow patterns in small channels are different from those in the big ones. Non-Taylor bubbles (with a bubble length L_b smaller than the tube diameter D_t) occur at low gas superficial velocities and high liquid superficial velocities. The length of Taylor bubbles increases quickly with increasing gas velocity and decreasing liquid velocity. The bubble front and rear shapes change with the Reynolds number (defined based on the two-phase velocity $U_s = U_{sl} + U_{sg}$). At low Re, both the bubble front and rear shapes show a hemispherical cap shape. With increasing Re, the radius of the curvature at the bubble tip becomes smaller and the rear cap becomes flattened.

The long Taylor bubbles at the bottom-right corner of Fig. 3 are formed by doubling (Taylor-pairing), where a growing bubble on the nozzle merges with the Taylor bubble in front of it. The boundary for Taylor-pairing to occur is given as $U_{sl} \leqslant 0.27U_{sg}$ based on the experimental data in [11]. This boundary is not accurate according to our calculations, as shown in Fig. 3. The calculated boundary is actually non-linear. In fact, the experimental range for U_{sl} was only up to 35 mm/s, and there were not enough data points to generate an exact boundary [11].

The process of Taylor-pairing is shown in Fig. 4 for $U_{sl} =$ 23 mm/s and $U_{sg} = 140$ mm/s. The second bubble which merges with the first one is much smaller. The merged bubble does not detach immediately, rather it keeps growing for about 7 ms before the detachment. The shape oscillation at the bottom of the bubble does not travel to the front of the Taylor bubble.

The bubble departure diameter decreases exponentially with the ratio of liquid and gas superficial velocities, as shown in Fig. 5. Taylor-pairing occurs for $U_{sl}/U_{sg} \leqslant 0.32$ within our cal-

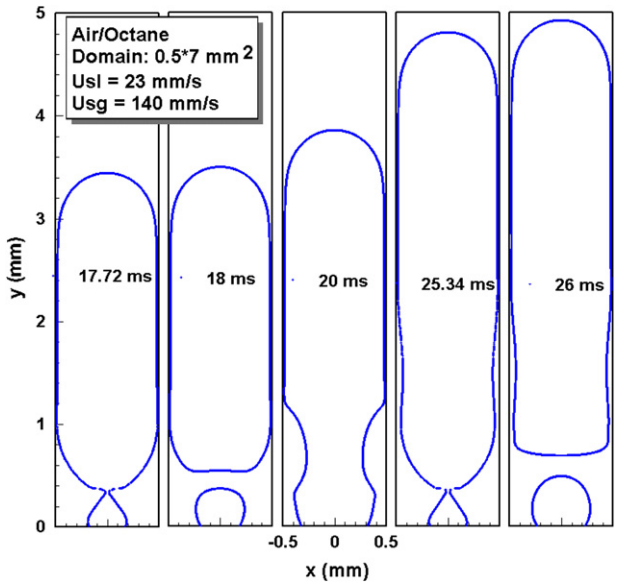

Fig. 4. Process of Taylor-pairing in front of the nozzle.

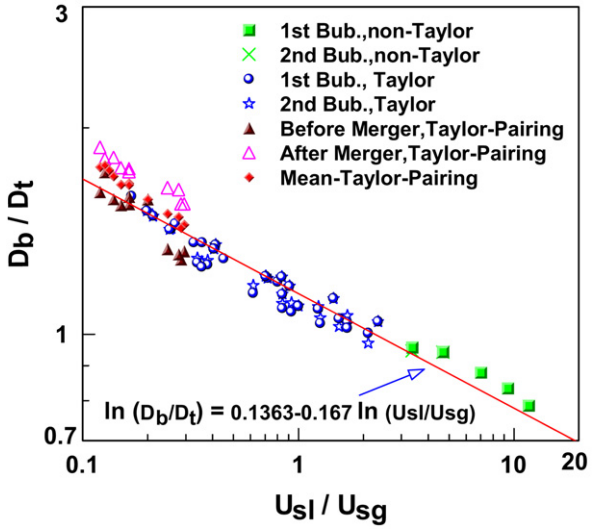

Fig. 5. Calculated bubble departure diameters vs. ratio of liquid and gas superficial velocities.

culation range. A fit of the calculated data (not including the Taylor bubbles after merger) gives

$$\ln(D_b/D_t) = 0.1363 - 0.167\ln(U_{sl}/U_{sg}) \quad (13)$$

Note that, Eq. (13) is obtained using the calculated data for one channel size only and it does not take into account the effects of physical properties.

3.3. Some properties of Taylor bubbles

Typically, a Taylor bubble is characterized by a sharp front nose and a relatively flattened bottom. The liquid film formed between the bubble and the wall is uniform at the middle part and the film thickness increases continuously towards the front nose while it shows somewhat wavy behavior towards the bottom (Fig. 6). Fig. 7 shows the thickness of the constant liquid film vs. the capillary number. The Bretherton's correlation (Eq. (1)) is also plotted in the figure. Note, that for the data shown in this study, the bubble length is generally smaller than 3 times the tube diameter. This may be the reason for the difference between the numerical calculations and Bretherton's predictions.

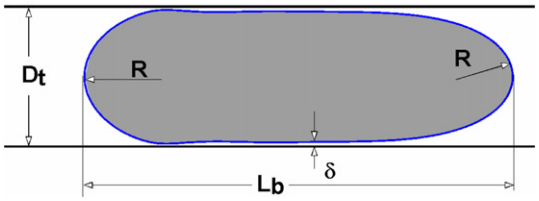

Fig. 6. Shape of a single Taylor bubble.

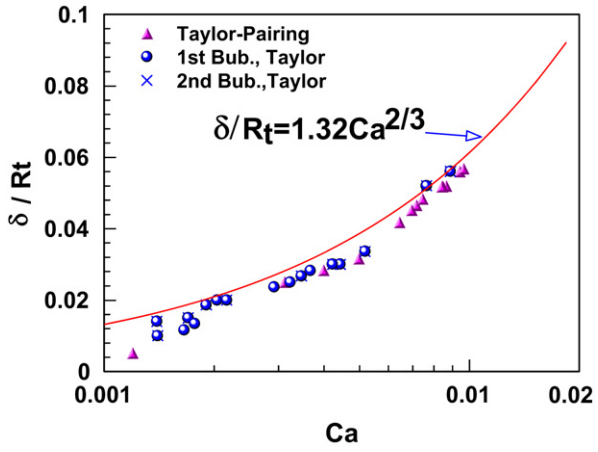

Fig. 7. Thickness of liquid film vs. capillary number.

For a known bubble equivalent diameter, we can roughly calculate the bubble length L_b by assuming that the both end caps of the bubble have a radius equal to $(D_t - 2\delta)/2$ (refer Fig. 6), i.e.

$$L_b/D_t = \frac{2}{3}(D_b/D_t)^3 + (1 - 2\delta/D_t) - \frac{2}{3}(1 - 2\delta/D_t)^3 \quad (14)$$

The Bretherton's correlation (Eq. (1)) can be used to calculate δ/D_t. Fig. 8 shows the calculated bubble length against the bubble diameter. Eq. (13) is used for comparison with the calculated bubble length. The maximum film thickness within the calculation range is $\delta/D_t < 0.06$. Therefore, we plot Eq. (14) for two extreme cases, i.e. $\delta/D_t = 0$ and $\delta/D_t = 0.06$. It can be seen that Eq. (14) can accurately predict the length of Taylor bubbles when L_b/D_t is larger than 2. For shorter bubbles, the length is underestimated since the mean liquid film thickness is higher than that given by the Bretherton's correlation.

The drift velocity of Taylor bubbles $(U_b - U_s)$ is much smaller than that for the non-Taylor bubbles, as shown in Fig. 9 in terms of the velocity ratio U_b/U_s vs. U_s. The calculations are compared with the experimental data of Kreutzer et al. [6] for an air/decane system in a capillary of 2.3 mm inner diameter. The physical properties of decane ($\rho = 730$ kg/m^3, $\mu = 0.000924$ Pa s, $\sigma = 0.024$ N/m) are very similar to those of octane. The predictions of Fairbrother and Stubbs [5] (Eq. (2)) and Bretherton [2] (Eq. (3) with a factor $(1 + 2/3Bo)$ for grav-

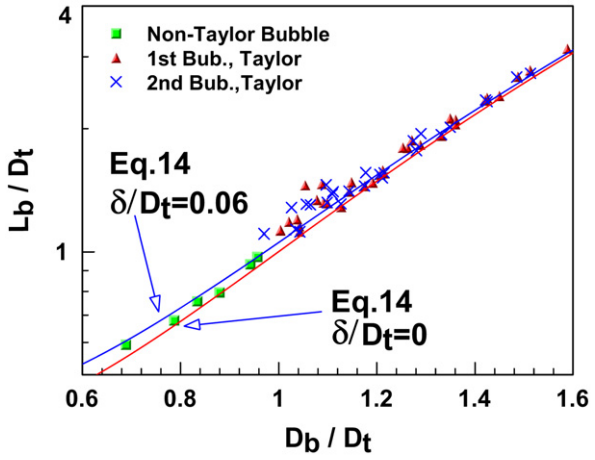

Fig. 8. Bubble length vs. bubble diameter.

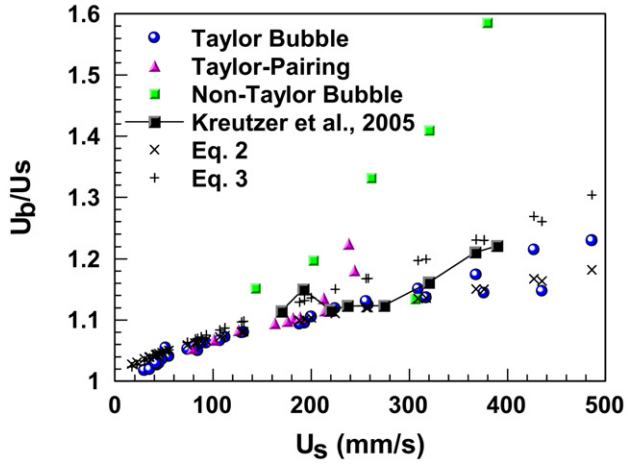

Fig. 9. Bubble rise velocity against two-phase velocity.

ity effect) are also shown in the figure. For Eqs. (2) and (3), we use the calculated bubble velocity for Ca, thus these two correlations are plotted as discrete data points. Eq. (3) (including the effects of the buoyancy force) predicts the upper limit of our calculations, and Eq. (2) gives the lower limit of the calculation data.

Other properties of Taylor bubbles such as flow recirculation and pressure drop will be discussed in the next section, since the calculations shown so far are for a relatively short calculation domain with y/x ranges from 10 to 12, and thus the flow field of the Taylor flow may not be fully developed.

3.4. Effects of nozzle geometry

In the previous sections, calculation results for a single nozzle geometry were presented. In this section, we will study the effects of nozzle geometry on the bubble formation for two given sets of liquid and gas superficial velocities, i.e. $U_{sl} = U_{sg} = 100$ mm/s and $U_{sl} = 50$ mm/s, $U_{sg} = 100$ mm/s. The tube inner diameter is kept unchanged (1 mm). The calculation domain now has a height/width ratio $y/x = 20$. The other parameters follow the same bench data given in Section 3.1.

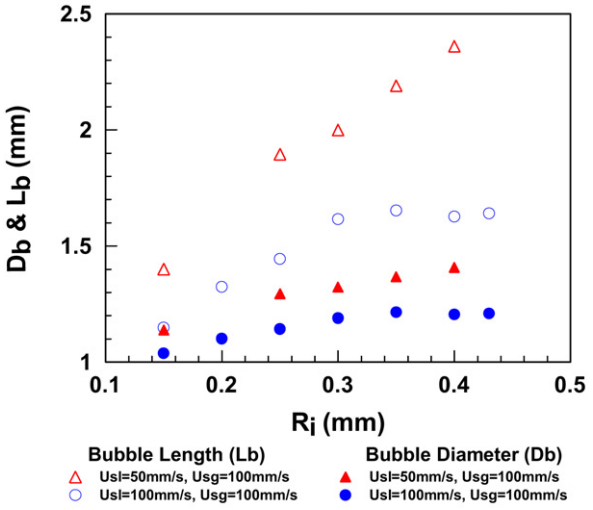

Fig. 10. Effects of nozzle geometry on bubble departure diameter and bubble length.

Fig. 10 shows the calculated bubble diameter (D_b) and bubble length (L_b) for different nozzle inner radii R_i with the same nozzle wall thickness of 0.05 mm. For $U_{sl} = U_{sg} = 100$ mm/s, the bubble diameter and thus the bubble length increase with increasing R_i from 0.15 to 0.35 mm, thereafter they remain almost constant. The maximum change in the bubble length is up to 44%. For $U_{sl} = 50$ mm/s and $U_{sg} = 100$ mm/s, both D_b and L_b increase with R_i. The maximum change in the bubble length is up to 70%.

The above results indicate that, under the same liquid and gas superficial velocities, the size of Taylor bubbles inside a given capillary can vary distinctly for different bubble generation devices. Therefore, the widely used flow pattern map presented in terms of liquid and gas superficial velocities (e.g., Fig. 3) is not unique. In other words, for a given set of U_{sl} and U_{sg}, different flow patterns can occur inside the same channel. This may be the reason that the experimental flow patterns are difficult to predict, since they are device dependent.

The change of the bubble length is interrelated to the change of the flow field, particularly, the change in the pressure drop behavior. The presence of bubbles in the liquid alters the velocity profiles and thus increases the heat and mass transfer between the liquid and wall, however, with a penalty of a pressure drop increment. The velocity field of a Taylor flow is shown in Fig. 11 with (a) for the absolute velocities, and (b) for the relative velocities. From Fig. 11(a), recirculation occurs only at the lower part of the bubble in the near-wall region. No recirculation can be seen inside the liquid slug. However, with U_s taken as the reference velocity (Fig. 11(b)), recirculations can be seen all along the channel with an alternative change of circulation direction as discussed in [9]. Several authors directly linked the heat and mass transfer enhancement to the recirculations within the liquid slugs, e.g., [23].

The change in pressure along the channel axis is shown in Fig. 12. The bubbles have a higher pressure than the ambient liquid slugs due to the Laplace pressure. There is a significant pressure drop across each bubble. The liquid pressure near the

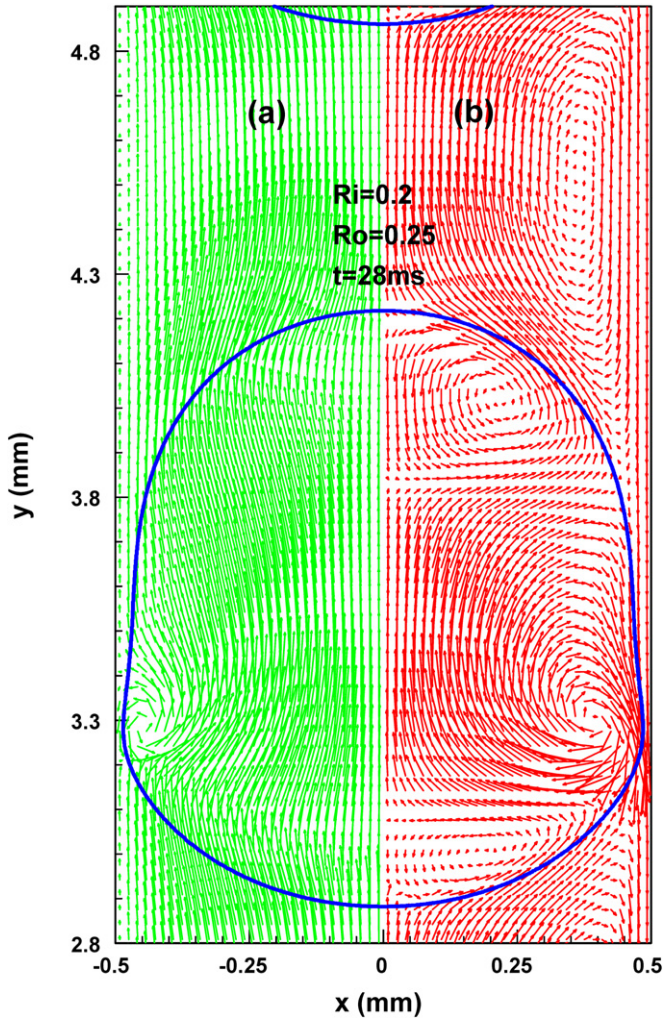

Fig. 11. (a) Absolute velocity field; (b) Velocity field with U_s as reference velocity ($U_{sl} = U_{sg} = 100$ mm/s).

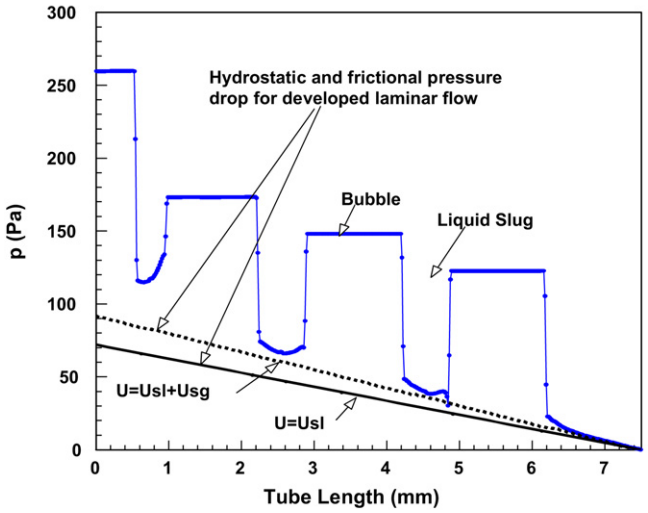

Fig. 12. Pressure along the tube axis (same conditions as those for Fig. 11).

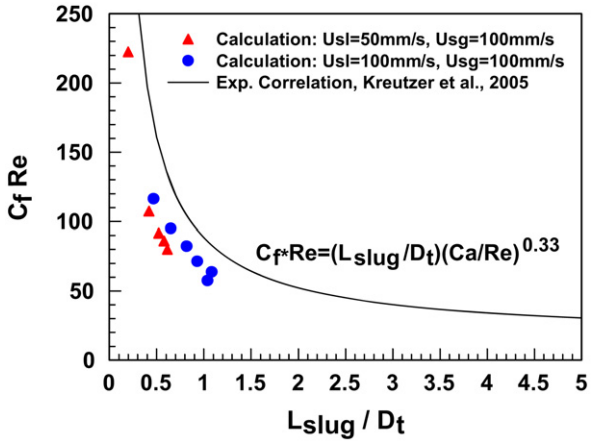

Fig. 13. Friction factor vs. slug length.

bubble interface is altered to deviate from the Hagen–Poiseuille law. The overall pressure drop of the Taylor flow is higher than the laminar single-phase flow of liquid with a velocity of U_{sl} (solid line in Fig. 12) or U_s (dashed line in Fig. 12).

The friction factor for the Taylor flow is calculated as

$$C_f = \left[(\Delta p/L)_{tot} - \rho_l g L \beta_l\right] / \left[(0.5\rho_l U_s^2)(4/D_t)\beta_l\right] \quad (15)$$

Here, $(\Delta p/L)_{tot}$ is the total pressure drop over a tube length of L. This term is calculated over a length of two neighboring bubble/slug units. β_l is the dynamic liquid hold-up which can be calculated by $L_s/(L_s + L_b)$ [6]. The results in terms of $C_f Re$ against the non-dimensional slug length are shown in Fig. 13. These results are compared with the experimental correlation given in [6] which was validated for a non-dimensional slug length (L_s/D_t) larger than about 2. From Fig. 13 we see a strong increase of the friction factor over the laminar single-phase flow ($C_f Re = 16$). With decreasing slug length (or increasing bubble length in this example), the friction factor increases quickly. Therefore, the use of different nozzles can lead to a change not only in the flow patterns but also in the pressure drop behavior. For practical applications, to maximize the gas–liquid interfacial area for a given gas/liquid flow rate, the nozzle size should be small which produces small bubbles, however the pressure drop per channel length is high. For the purpose of reducing the pressure drop, the larger nozzle is preferred, from which longer bubbles are generated.

4. Conclusions

Numerical simulations have been carried out for the transient formation of Taylor bubbles in a nozzle/tube co-flow arrangement. The calculated bubble diameters agree quite well with the experimental data. The Taylor bubble formation in a liquid co-flow is found to be weakly dependent on the contact line dynamics which is not the case for bubble formation in a quiescent liquid. The bubble size can be well correlated to the ratio of liquid and gas superficial velocities. The calculated bubble shape, liquid film thickness, bubble length, drift velocity, pressure drop and flow fields of Taylor flow all agree reasonably well with the literature data.

It was also shown numerically that under the same liquid and gas superficial velocities, the size of Taylor bubbles inside a given capillary, and thus the pressure drop behavior can vary strongly for different bubble generation devices. Therefore, the

widely used flow pattern map presented in terms of liquid and gas superficial velocities is not unique and insufficient.

References

[1] G. Bercic, A. Pintar, The role of gas bubbles and liquid slug lengths on mass transport in the Taylor flow through capillaries, Chem. Eng. Sci. 52 (1997) 3709–3719.

[2] F.P. Bretherton, The motion of long bubbles in tubes, J. Fluid Mech. 10 (1961) 166–168.

[3] G. Taylor, Deposition of a viscous fluid on the wall of a tube, J. Fluid Mech. 10 (1961) 161–165.

[4] M.D. Giavedoni, F.A. Saita, The rear meniscus of a long bubble steadily displacing in a Newtonian liquid in a capillary tube, Phys. Fluids 11 (1999) 786–794.

[5] F. Fairbrother, A.E. Stubbs, Studies in electroendosmosis. VI. The "bubble tube" method of measurement, J. Chem. Soc. 1 (1935) 527–529.

[6] M.T. Kreutzer, F. Kapteijn, J.A. Moulijn, C.R. Kleijn, J.J. Heiszwolf, Inertial and interfacial effects on pressure drop of Taylor flow in capillaries, AIChE J. 51 (2005) 2428–2440.

[7] T. Taha, Z.F. Cui, Hydrodynamics of slug flow inside capillaries, Chem. Eng. Sci. 59 (2004) 1181–1190.

[8] T.C. Thulasidas, M.A. Abraham, R.L. Cerro, Flow patterns in liquid slugs during bubble-train flow inside capillaries, Chem. Eng. Sci. 52 (1997) 2947–2962.

[9] M. Heil, Finite Reynolds number effects in the Bretherton problem, Phys. Fluids 13 (2001) 2517–2521.

[10] A. Bhunia, S.C. Pais, Y. Kamotani, I.H. Kim, Bubble formation in a coflow configuration in normal and reduced gravity, AIChE J. 44 (1998) 1499–1509.

[11] W. Salman, A. Gavriilidis, P. Angeli, On the formation of Taylor bubbles in small tubes, Chem. Eng. Sci. 61 (2006) 6653–6666.

[12] S. Osher, J.A. Sethian, Fronts propagating with curvature-dependent speed: algorithms based on Hamilton–Jacobi formulations, J. Comp. Phys. 79 (1988) 12–49.

[13] M. Sussman, E. Fatemi, P. Smereka, S. Osher, An improved level set method for incompressible two-phase flow, Comput. Fluids 27 (1998) 663–680.

[14] M. Sussman, E. Fatemi, An efficient, interface preserving level set redistancing algorithm and its application to interfacial incompressible flow, SIAM J. Sci. Comp. 20 (1999) 1165–1191.

[15] J.U. Brackbill, D.B. Kothe, C. Zemach, A continuum method for modeling surface tension, J. Comp. Phys. 100 (1992) 335–354.

[16] A. Chorin, Numerical solution of the Navier–Stokes equations, Math. Comp. 22 (1968) 745–762.

[17] C.-W. Shu, High-order finite difference and finite volume WENO schemes and discontinuous Galerkin methods for CFD, Int. J. Comp. Fluid Dyn. 17 (2003) 107–118.

[18] K.A. Smith, J.M. Ottino, P.B. Warren, Simple representation of contact-line dynamics in a level-set model of an immiscible fluid interface, Ind. Eng. Chem. Res. 44 (2005) 1194–1198.

[19] H. Huang, D. Liang, B. Wetton, Computation of a moving drop/bubble on a solid surface using a front-tracking method, Comm. Math. Sci. 2 (2004) 535–552.

[20] M. Francois, W. Shyy, Computations of drop dynamics with the immersed boundary method, Part 2: Drop impact and heat transfer, Numer. Heat Transfer 44 (2003) 119–143.

[21] Y. Chen, R. Mertz, R. Kulenovic, Effects of contact angle for bubble formation on submerged orifices, in: Int. Conf. on Multiphase Flow, Leipzig, Germany, July 9–13, 2007.

[22] M. Pasandideh-Fard, Y.M. Qiao, S. Chandra, J. Mostaghimi, Capillary effects during droplet impact on a solid surface, Phys. Fluids 8 (1996) 650–659.

[23] S. Irandoust, B. Andersson, Liquid film in Taylor flow through a capillary, Ind. Eng. Chem. Res. 28 (1989) 1684–1688.